DENTAL MATERIALS 37 (2021) 1698–1713

Available online at www.sciencedirect.com

ScienceDirect

journal homepage: www.intl.elsevierhealth.com/journals/dema

Melatonin-doped polymeric nanoparticles induce high crystalline apatite formation in root dentin

Manuel Toledano-Osorio[a], *Fátima S. Aguilera*[a], *Esther Muñoz-Soto*[a], *Estrella Osorio*[a], *Manuel Toledano*[a,*], *Germaine Escames*[b], *Antonio L. Medina-Castillo*[c], *María T. Osorio*[e], *Modesto T. López-López*[d], *Marta Vallecillo-Rivas*[a], *Raquel Osorio*[a]

[a] *University of Granada, Department of Stomatology, Colegio Máximo de Cartuja s/n, Granada 18071, Spain*
[b] *Faculty of Medicine, Department of Physiology, Biomedical Research Center, CIBERFES, Ibs. San Cecilio University Hospital, University of Granada, Granada, Spain*
[c] *University of Granada, NanoMyP, Spin-Off Enterprise, Edificio BIC-Granada, Av. Innovación 1, 18016, Armilla, Granada, Spain*
[d] *University of Granada, Faculty of Science, Applied Physics Department, Av. Fuente Nueva s/n, 18071 Granada, Spain*
[e] *Independent Research Scholar, Granada, Spain*

ARTICLE INFO

Article history:
Received 27 July 2021
Accepted 4 September 2021

Keywords:
Apatite
Dentin
Hardness
Melatonin
Polymeric nanoparticles
Remineralization
Transmission electron microscopy
X-ray diffraction

ABSTRACT

Objective. To investigate the effect of novel polymeric nanoparticles (NPs) doped with melatonin (ML) on nano-hardness, crystallinity and ultrastructure of the formed hydroxyapatite after endodontic treatment.

Methods. Undoped-NPs and ML-doped NPs (ML-NPs) were tested at radicular dentin, after 24 h and 6 m. A control group without NPs was included. Radicular cervical and apical dentin surfaces were studied by nano-hardness measurements, X-ray diffraction and transmission electron microscopy. Mean and standard deviation were analyzed by ANOVA and Student-Newman-Keuls multiple comparisons ($p < 0.05$).

Results. Cervical dentin treated with undoped NPs maintained its nano-hardness values after 6 m of storage being [24 h: 0.29 (0.01); 6 m: 0.30 (0.02) GPa], but it decreased at apical dentin [24 h: 0.36 (0.01); 6 m: 0.28 (0.02) GPa]. When ML-NPs were used, nano-hardness was similar over time [24h: 0.31 (0.02); 6 m: 0.28 (0.03) GPa], at apical dentin. Root dentin treated with ML-NPs produced, in general, high crystallinity of new minerals and thicker crystals than those produced in the rest of the groups. After 6 m, crystals became organized in randomly oriented polyhedral, square polygonal block-like apatite or drop-like apatite polycrystalline lattices when ML-NPs were used. Undoped NPs generated poor crystallinity, with preferred orientation of small crystallite and increased microstrain.

Significance. New polycrystalline formations encountered in dentin treated with ML-NPs may produce structural dentin stability and high mechanical performance at the root. The

* *Corresponding author.*
E-mail address: toledano@ugr.es (M. Toledano).
https://doi.org/10.1016/j.dental.2021.09.001

decrease of mechanical properties over time in dentin treated without NPs indicates scarce remineralization potential, dentin demineralization and further potential degradation. The amorphous stage may provide high hydroxyapatite solubility and remineralizing activity.

1. Introduction

Conventional treatment methods in dental pulp inflammation, apical periodontitis and irreversible pulpitis comprise the pulp chamber disinfection plus filling with biomaterials. This is generally recognized as root canal treatment [1]. Inflammation is always associated with the production of reactive oxygen species. It has been demonstrated that, in several endodontic pathologies such as periapical abscess and pulpitis, oxidative stress is an important pathogenic mechanism [2,3]. The free radicals that generate reactive oxygen or nitrogen species, through oxidative stress, are considered to be highly destructive, but directly neutralized by melatonin (ML) [4]. The role of ML in hard tissues has claimed attention [5]. ML (*N*-acetyl-5-metoxy-tryptamine) is an indoleamine that is synthesized and secreted by the pineal gland in a circandian pattern [4]. Melatonin is also formed in perhaps all organs in quantities by orders of magnitude higher than in the pineal gland and in the circulation [6]. ML is involved in the development of teeth [7] and may also regulate dentin formation.

One of the goals for regeneration of dentin-pulp complex is to reconstruct the pulp repair capability by mineralization [3]. In bioactive molecules related with growth factors, transforming growth factor-β (TGF-β) shows a pivotal role. Ectopic mineralization in pulp tissue is inducted by TGF-β3, increasing type1 collagen levels and osteocalcin [8]. To treat pulpal inflammation, and to preserve or regenerate vital dental pulp, resolvines (RvE1 and RvD1), molecules coming from omega-3 polyinsatured fatty acids, have been recommended. Initial inflammatory responses are resolved by RvE1, which decreases NF-κβ, permitting macrophages in M1 stage to change to M2 stage. Special roles in standard morphogenesis of teeth are played by Wnt signaling molecule family. Wnt1, a step of Wnt/β-catenin signaling pathway interferes with the differentiation of the stem cells of dental pulp (DPSCs) into odontoblasts and inhibits ALP activity [9]. Signaling pathway is understood as the ability of cells to receive, process, and transmit signals with its environment and with itself [10,11]. All these strategies in handling signaling pathways for healing of dentin-pulp complex are representative of sophisticated, costly and uncertain approaches of tissue engineering for dentin repair [12]. Their effectiveness in regeneration of the dentin-pulp complex should be investigated further.

Although the benefits of ML on periodontal regeneration has been demonstrated in gingival fibroblasts and *in vivo* and *in vitro* animal models [13], its effects in radicular dentin regeneration have not been reported yet. Polymeric nanoparticles (NPs) with anionic carboxylate (*i.e.*, COO^-) groups located along the polymer support, that may be doped with ML (ML-NPs) have been previously synthesized to favor remineralization of dentin in endodontically treated teeth. Remineralization of radicular dentin may be a determinant factor trying to mechanically reinforce the tissue [14]. Non-resorbable polymeric NPs doped with antimicrobials and reinforcing agents have successfully been tested in advance [15], but combined anti-inflammatory, antioxidant, free-radical-scavenger and cytoprotective properties therapy have only been partially considered [12,13,16–18].

Dentin, a mineralized connective tissue, constitutes the main part of dental organ. It is made of 70% (by weight) inorganic calcium deficient hydroxyapatite (HAp) crystal in the form of a sub-micrometer to nanometer-sized carbonate rich with crystallites (~5 × 30 × 100 nm) [19]. This nanocrystalline hydroxyapatite is partitioned into extrafibrillar and intrafibrillar mineral, accounting the later for the maintenance of the mechanical properties [20]. Crystallites determine the mineral content of dentin, whose maturity, texture and size are influenced by their tooth location [21,22]. Both morphology and dimensions of the formed HAp crystallites influence its clinical service and mechanical properties [23]. Dentin is characterized by its hierarchical structure that can accurately be analyzed by X-ray diffraction (XRD), providing data of lattice strain on the tooth surface and crystal orientation of crystallites [24]. High resolution transmission electron microscopy (HRTEM) and selected area diffraction patterns (SAED) measure shape, size and dentin nanostructures. Elemental constituents through energy dispersive X-ray spectroscopy analysis (EDX) can also provide information about the chemical composition of crystallites. Root dentin does have regional variations in its material properties. There exists a decreasing tendency in mineral presence from the cervical to the apical region, and this mineral content will condition both clinical and mechanical performance of root dentin [25].

Thus, the purpose of the present study was to determine the influence of crystallinity, amorphization, crystallite and gran size, lattice strain and texture on nanohardness (*Hi*) and remineralization of radicular dentin after ML-NPs treatment. The challenge is to ascertain if *Hi* increases after NPs application. The *Hi* rise is directly associated to a higher presence of intrafibrillar mineralization and improved tissue maturation [26,27]. The research question that guided the present study was: Does melatonin-doped polymeric nanoparticles application improve crystallinity and maturity in radicular dentin? The null hypothesis is that ML-NPs application in the inner wall of the root canal did not affect, at the short term or overtime, nanohardness, crystal morphology and structure of radicular dentin.

2. Materials and methods

2.1. Nanoparticles fabrication and characterization

PolymP-*n* Active nanoparticles (NPs) (NanoMyP, Granada, Spain) have been synthesized through polymerization precipitation by the Flory-Huggins model, using a 14 mL Nalgene® plastic bottle to mix0.170 mL of ethylene dimethacrylate (EDMA), 0.045 mL of methacrylic acid (MAA), 0.137 mL of hydroxyethylmethacrylate (HEMA) and 14 mL of solvent. Then, 8.75 mg of azobis-isobutyronitrile (AIBN) were added and the system was sonicated during 1 min, the mixture was cooled at −8 °C and the O_2 was removed by purging the system whit a soft flow of N_2 during 3 min [28]. The NPs are composed of ethylene glycol dimethacrylate as the cross-linker, the methacrylic acid as the functional monomer and 2-hydroxyethyl methacrylate as the backbone monomer. NPs were functionalized with melatonin.

The NPs ML loading process was conducted by immersion of 150 mg of NPs in 15 mL of distilled water melatonin solutions (containing 50 mg of melatonin) for 2 h at room temperature under constant shaking. The NPs were then left at room temperature until de solvent was completely evaporated, ensuring that all the ML remains adhered to the NPs. ML is electrostatically immobilized on the NPs surface (acid-base interaction). The secondary amino groups (R_2NH) of melatonin interacted with the carboxyl groups (COOH) present on the NPs surface. ML loading on NPs was previously probed to be 0.33 mg of ML per mg of NPs. The melatonin liberation profile was also calculated and it is about 1.85 mg/mL at 24 h to 0.033 mg/mL at 28 d [12].

Then, a suspension of 5 mg /mL of NPs-Melatonin in water was prepared and the size and Z potential (ζ) were measured by triplicate by Dynamic Light Scattering (DLS) using a Zetasizer Nano ZS90 (Malvern Instrument Ltd, Malvern, UK).

For TEM characterization of the NPs, a specific amount of the diluted sample was put on the mesh copper grid coated with activated carbon, and then dried. Before observation, this sample was negatively stained with uranyl acetate (2%) [29,30]. Images were acquired on a TEM ThermoFisher Scientific TALOS F200X (Thermofischer, Waltham, MA, USA) microscope, working at 200 kV.

Fourier-transform infrared spectroscopy (FTIR) characterization was also performed for NPs, ML-NPs and ML. Samples were analyzed on a JASCO 6200 FTIR (frequency range 400–4000 cm^{-1}, 2 cm^{-1} spectral resolution and 75 scans) equipped with an diamond-tipped attenuated total reflectance (ATR) device (ATR Pro ONE, JASCO Inc., Maryland, USA) for spectra collection without sample preparation, minimizing artifacts [31].

Two types of NPs were included in the study undoped-NPs and ML-doped NPs (ML-NPs).

2.2. Teeth specimen preparation and nanoparticles application

Donors (18–25 yr of age) provided thirty-six sound human mandibular premolars, with informed consent and following the Declaration of Helsinki [Institution Review Board (#405/CEIH/2017)].

A low-speed diamond saw (Accutom-50 Struers, Copenhagen, Denmark) under constant water irrigation was used to decoronate the samples at the cemento-enameljunction. Parameters that were followed are: root length 12 mm and checking with 2 angulations X-ray of a single canal presence. The treatment of the root canal started with the use of Gates Glidden drills (Dentsply Maillefer, Ballaigues, Switzerland), size 2 and 3, to shape the roots coronal third part. Afterwards, the canal patency was achieved with a size 15 Flex-o-file (Dentsply Maillefer, Ballaigues, Switzerland). The working length was verified, and it was established 0.5 mm shorter than apical foramen. ProTaper nickel-titanium rotary instruments (Dentsply Maillefer, Ballaigues, Switzerland) were used for the final instrumentation (<size F4). Each time the instrument was changed, the root canal was irrigated with 0.5 mL of 5% sodium hypochlorite (NaOCl, Panreac, ref. n. 212297), while at the end of canal instrumentation 0.5 mL of a 17% EDTA solution were used for 3 min (MD-Cleanser, Meta Biomed, Chungbuk, Republic of Korea) to remove the smear layer. All specimens were finally irrigated with 0.5 mL of 5% NaOCl for 1 min, followed with distilled water for one more minute, and then dried with paper points (Dentsply Maillefer) [32]. A random distribution for specimens was established in 3 groups (n = 12). The teeth roots received 100 μl of the two distinct ethanol suspensions of NPs at 10 mg/ml. NPs were not applied in the control group, but just 100 μl of ethanol. Subsequently, in all groups, AH-Plus sealant cement (Dentsply Maillefer, Ballaigues, Switzerland) was introduced into the instrumented root canal with a lentulo spiral and, immediately, one size 30 guttapercha cone (Guttacore, Dentsply Maillefer, Ballaigues, Switzerland) was placed and compacted to working length into the canal, in all groups, to complete the obturation. Finally, the excess of gutta-percha and/or cement was removed from the coronal portion of the root canal, and the specimens were obturated with Cavit. (ESPE, 3M, St. Paul, MN, USA) as a provisional restoration [33]. The control group was the group without NPs application and only AH-Plus was applied. AH-Plus was also applied for the rest two groups. All procedures were conducted by the same operator. Two periods of study were established at 24 h or 6 m. After storage, two dentin discs, representative of cervical and apical radicular dentin were cut at 12.5 and 2.5 mm above apex, respectively at each specimen (Fig. S1).

2.3. Nanoindentation

Dentin surfaces were polished with silicon carbide (SiC) abrasive discs from 600 to 4000 grit mounted on water-cooled polishing equipment (LaboPol 4, Struers, Copenhagen, Denmark). Then, the specimens were finally submitted to an ultrasonic cleaning procedure during 10 min to eliminate the created dentin debris during the polishing procedure. A Hysitron Ti-750D TriboIndenter (Hysitron, Inc., Minneapolis, MN) with a commercial nano-DMA package was used in this research. A Berkovich (three sides pyramidal) diamond tip (tip radius ~20 nm) was the nanoindenter. Ten nanoindentations were executed on each slab (cervical and apical root dentin) at 20 μm next to the radicular canal, at the region of inter-

est (Fig. S1). The rest of the nanoindentation procedure was as in Toledano et al. [32]. Data were analyzed with ANOVA and Student-Newman-Keuls multiple comparison tests, with statistical significance preset at $p < 0.05$.

2.4. X-ray diffraction (XRD) analysis

An X-ray microdiffractometer (μXRD^2) Bruker-D8 Venture (Bruker AXS, Karlsruhe, Germany) provided with a 2-dimensional detector CMOS Photon 100 (Bruker AXS, Karlsruhe, Germany) and a kappa geometry based goniometer 2D Detector was used for the analysis. The X-ray beam (λ = 1.5418 Å, Cu Kα line) was produced by a Cu microforms supply IμS. Settings generator were 50 kV/1 mA. The position-sensitive 2D detector used was 1024 × 1024 pixels. Beam collimator diameter was 0.1 mm (spot size 100 μm) and its length 90 mm. The detector distance to crystal was calibrated with a sample of ylid. The sample was fixed on the XYZ goniometer with the surface to be analyzed placed normal to the φ axis. Then the goniometer is automatically adjusted to bring the sample surface into focus, with the region of interest in the center of the crosshair of the video window by means of a video camera system (NTSC-Digital Video Camera. Model LCL-211H, Watec America Corp.,USA). The considered kappa goniometer positions at 40 mm distance were: 2θ, 40°; ω, 20°; φ, 270°; χ, 50°. The exposure time was 60.00 s and the measurements were performed at room temperature (295 ± 0.1 °K). Three images were obtained from each specimen. The final refined μXRD^2 profile and Debye–Scherrer rings image (pole image) of each group were obtained by accumulating all X-ray energies (wavelengths) in a single image. The results are commonly presented as maximum positions in 2θ (x) and X-ray counts (intensity) (y) in the form of an x–y chart. The XRD^{2}DScan software [34] was employed, as it allows all images to be integrated into a representative single image. The whole batch of the measured frames is loaded and all frames are processed; then a single file is created. This file contains the variation of intensity along the Debye ring associated with the selected reflection as a function of angle, for every processed frame. All this information was used to construct the final refined μXRD^2 profile and pole image.

The X-ray microdiffraction pattern was used to calculate the preferred orientation and size of the crystallites [35,36]:

$$d = \frac{K\lambda}{\beta \cos\theta} \quad (1)$$

were d indicate the mean size of the crystallites, K is defined as a dimensionless form factor and presents a value near unity-note that in dentin it is $K \approx 0.94$- [36], and β corresponds to the peak full width at half maximum (FWHM) of the line broadening.

This equation was used for the broadenings of the 002 (H) and 310 (L) reflections, to evaluate the crystallite length and width, respectively. The highest peak (112) was also measured. Crystallites preferred orientation, *i.e.*, the texture, was calculated from the next intensity ratios [36]:

$$R_{hkl} = k_{hkl} \frac{I_{211}}{I_{hkl}} \quad (2)$$

In this equation, I_{hkl} and I_{211} were respectively the intensities of the line reflections hkl and 211, and

$$k_{hkl} = \frac{I^{st}_{hkl}}{I^{st}_{211}} \quad (3)$$

In this formula, *st* indicate the intensities obtained following to the JCPDS card [36].

2.5. High resolution transmission electron microscopy (HRTEM), energy dispersive X-ray spectroscopy (EDX) analyses of dentin discs

Dentin discs (1 mm thickness) were perpendicularly sectioned at three points: (1) in the middle, (2) about 500 μm to the right of the interface and the same distance to the left. The external surfaces (cementum) of the specimens were polished until a 100 μm distance from the interface. SiC abrasive papers, from 600 until 2400 grit were used for grinding (Buehler-MetaDi, Buehler Ltd. Lake Bluff, IL, USA). Then, the specimens were finally submitted to an ultrasonic cleaning procedure during 10 min (Fig. S1) to eliminate the created dentin debris. A fine-grained powder was obtained after milling each dentin specimen. Afterwards, 2 mL of an aqueous solution of NaOCl (2%) was added to the dentin powder in order to eliminate the collagen, the process was completed under a sonicator (Ultrasons HD, P. Selecta SA, Barcelona, Spain) during 1 week. NaOCl solution was replaced each 24 h. The rest of the procedures was as in Martínez-Ruiz et al. [37]. A SUPER-X silicon-drift windowless EDX detector, for analytical electron microscopy (AEM), was also used. Digital X-ray maps and selected area electron diffraction (SAED) was employed on HAp particles. Nanoindentation, XRD, HRTEM and EDX analyses were executed at 24 h and 6 m of SBFS storing.

3. Results

3.1. Nanoparticles fabrication and characterization

The size of the unloaded NPs was 242.3 ± 20 nm. The polydispersity index (PDI) was 0.050 ± 0.003, and the zeta potential (ζ) is 38.5 ± 1.0 mV. The size of NPs loaded with ML, measured by DLS was 292.3 ± 30 nm, with a PDI 0.230 ± 0.08. The zeta potential (ζ) was 24.5 ± 0.5 mV.

TEM images of NPs are displayed in Fig. 1. NPs presented a spherical shape and did not agglomerate. No differences in morphology were found after melatonin loading.

FTIR-bands of the melatonin and NPs overlapped, and the amine and amide groups of melatonin could not be identified in the FTIR spectrum of ML-NPs (Fig. S2).

3.2. Nanoindentation

Mean and SD of nanohardness (*Hi*) at both cervical and apical dentin are shown in Fig. 2. All specimens, regardless the group, performed similar when cervical root dentin was analyzed at 24 h. Samples treated with undoped NPs attained higher *Hi* than the rest of the groups at apical root dentin, at 24 h of storage. After 6 m time point, all NPs-based groups showed

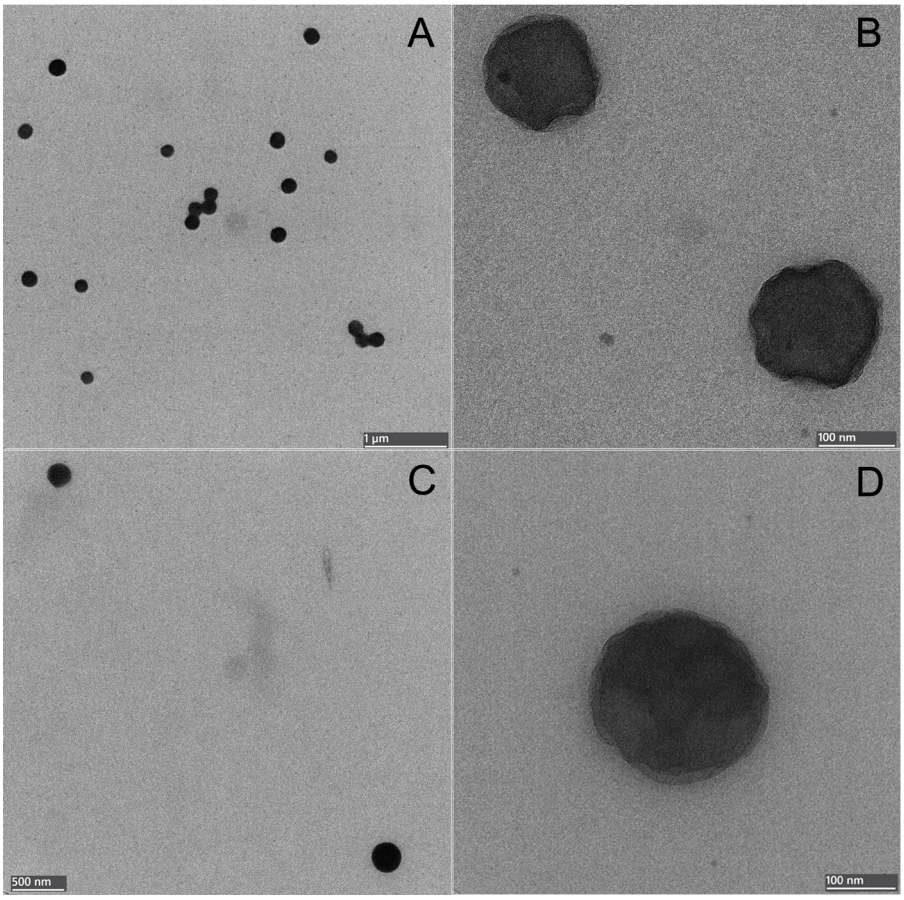

Fig. 1 – Transmission electron microscopic (TEM) images of undoped nanoparticles (NPs) and melatonin-doped NPs (ML-NPs). Dark and light objects inside the NPs were artifacts that developed during electron beam transmission. Scale bars are 1 μm (A), 100 nm (B, D) and 500 nm (C) in total length.

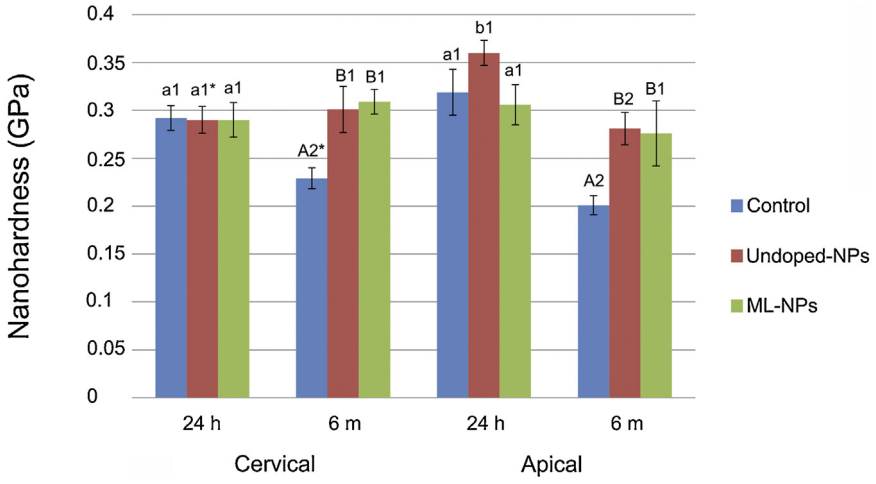

Fig. 2 – Mean and standard deviation (SD) values of nanohardness, *Hi*, (GPa) attained at the different experimental groups. Identical lowercase means no significant difference among distinct NPs at the same dentin half (cervical and apical) at 24 h. Identical capital letter indicates no significant difference between different NPs at the same dentin half (cervical and apical) at 6 m. Identical number indicates no significant difference between different storage time (24 h *vs* 6 m) within the same NPs at the same dentin half (cervical and apical). Asterisks indicate significant difference between different dentin halves (cervical vs apical) within the same NPs at the same storage time (24 h and 6 m).

higher *Hi* than the control group. Samples without NPs showed *Hi* decrease over time, irrespective of the dentin location. Cervical dentin treatment with undoped NPs maintained its *Hi* after 6 m, but *Hi* decreased at apical dentin. When ML-NPs were employed, Hi did not change over time, regardless of the dentin location (Fig. 2).

3.3. *X-ray diffraction (XRD) analysis*

Physical broadening (FWHM) of peaks at 002 achieved the highest (more amorphous) and lowest (more crystalline) values at cervical and apical dentin surfaces submitted to treatment with undoped NPs, respectively at 6 m of immersion (Table 1). Peaks at 310, after 6 m, presented the lowest FWHM at cervical and apical dentin treated with ML-NPs, denoting a crystalline status (Table 1). The highest peak (112) showed the maximum FWHM (more amorphous) at cervical dentin treated with ML-NPs, after 6 m of storage. At 24 h, the highest crystallinity was achieved at cervical dentin treated with ML-NPs (Table S1). Cervical dentin treated with ML-NPs at 6 m time point, showed a typical reflection at 002 peak (Fig. 3A inset) and diffraction rings that corresponded to 002 plane, with higher crystallinity values than samples treated with undoped NPs (Table 1) (Fig. 4B, C). At apical dentin and 310 plane, the highest crystallinity (lowest FWHM) (Fig. 3B inset) was obtained with dentin treated with ML-NPs, that also unveiled the brightest rings on most peaks (Fig. 4F).

After 6 m of immersion, cervical dentin specimens treated with ML-NPs showed higher FWHM values (more amorphous) than at 24 h of storage at both 002 and 310 planes. At apical dentin and 310 plane, crystallinity increased (lower FWHM) over time (Fig. S3). The highest peak (112) showed an increase of crystallinity after comparison between 24 h and 6 m when assessing the control group and cervical dentin treated with undoped-NPs (Table S1). The Fig. S4 represented the highest XRD peak of apical dentin treated with ML-NPs after 6 m of storage.

3.3.1. *Crystallite and grain size assessment*

A scattering dominion of the crystallite size is shown in Table 1. Apical dentin treated with undoped-NPs attained the longest crystallite size [τ_{002} (*H*)] (23.54 nm). Cervical and apical dentin treated with ML-NPs achieved the widest [τ_{310} (*L*)] (6.62 and 6.85 nm) crystallite size, respectively, after 6 m.

At 310 reflexions, the highest values of grain size occurred when treating both cervical and apical dentin with ML-NPs (6.24 and 6.46 nm, respectively) (Table 1).

3.3.2. *Microstrain assessment*

The shortest dimension of the lattice strain (002 reflection) corresponded to diffractions performed in specimens treated with ML-NPs at cervical (1.6×10^{-6}) and apical dentin (1.1×10^{-6}), at 6 m (Table 1). ML-NPs, at 310 reflexions, attained the lowest strain at both cervical and apical dentin (1.3×10^{-5} and 1.2×10^{-5}, respectively) (Table 1).

3.3.3. *Texture and H/L ratio assessments*

At cervical dentin and at 002 plane (6 m), the texture showed the trend ML-NPs > AH-Plus > undoped NPs. The apical region revealed the trend ML-NPs > AH-Plus > undoped NPs. Cervical dentin, at 310 plane acted as follows: AH-Plus > undoped NPs > ML-NPs, and at apical dentin the trend followed the sequence: undoped NPs > AH-Plus > ML-NPs (Table 1). The lowest *H/L* quotient was obtained in samples treated with ML-NPs at both apical and cervical dentin (Table 1).

3.4. *High resolution transmission electron microscopy (HRTEM), energy dispersive X-ray spectroscopy (EDX) analyses, and Fourier transform infrared (FTIR) characterization of NPs*

Representative examples of HRTEM are included Figs. 5, 6 and 7. At 24 h, samples treated with ML-NPs showed, at cervical root dentin, mainly starry needle-like apatite crystals (Fig. 5A), meanwhile apical root dentin showed preferentially parallelized alignments crystals (Fig. 5B). The electron diffraction analysis showed the typical amorphous structure of crystals (Fig. 5C, D). The observed crystal sizes usually range from 100–200 nm.

At 6 m of storage and HRTEM/EDX analysis, samples treated with ML-NPs showed structures organized in plate, needle and block-like apatite polygons (Fig. 6A) of polycrystalline nature (Fig. 6B), when cervical root dentin was analyzed. Similar treatment in apical dentin produced polyhedral, squared or drop-like shaped apatite crystals, crystalline in nature from a mineralogical and crystallographic standpoint (Fig. 7D–H). Diffraction patterns showed *d*-spacing values and clear central halo rings, indicating crystallinity (Fig. 6B, F, H). The observed crystal sizes usually range from 100–200 nm. Energy dispersive X-ray (EDX) detected Ca and P as part of the elemental analysis (Fig. 6I).

HRTEM analysis, at 6 m, of samples treated with AH Plus showed structures organized in typical polymorph/polyhedral apatite crystals shaped by plate-like overlapped polygons (Fig. 7A) amorphous in nature (Fig. 7B), when cervical root dentin was analyzed. The selected area electron diffraction (SAED) image obtained showed amorphous precipitates in the apatite particles, as diffractography depicted diffuse halo rings, indicating mineral amorphization (Fig. 7B). At 6 m of immersion and HRTEM analysis, samples treated with undoped NPs presented semi-crystalline structures ordered in block-like crystallite morphology when apical root dentin was analyzed (Fig. 7C). These analyses permit to observe apatite crystals and particles with relative crystalline profile (Fig. 7D). The SAED (selected area electron diffraction image) obtained showed well-crystallized apatite though with diverse degree of crystallinity (Fig. 7D). The characteristic *d*-spaces were clearly determined. The observed crystal sizes usually ranged from 100–200 nm.

4. Discussion

Dentin treated with ML-NPs conserved its original nanohardness values after 6 m of storage and showed, in general, higher crystallinity than samples treated with undoped NPs. Thicker crystallites appeared randomly oriented showing multivariate morphologies that ranged from polyhedral or square polygonal block-like apatite to drop-like apatite polycrystalline lattices. Any type of dentin treated with ML-NPs

Table 1 – Micro-X-ray diffraction pattern analysis approach of the experimental groups.

	Disc	Storage time	002 plane					310 plane					*H/L*
			FWHM	*H*: Scherrer equation (nm) (τ)	Scherrer-Wilson equation (nm)	Microstrain %	R_{hkl}	FWHM	*L*: Scherrer equation (nm) (τ)	Scherrer-Wilson equation (nm)	Microstrain %	R_{hkl}	
Control	Cervical	24 h	0.0081	18.26	17.80	1.6×10^{-6}	0.525	0.0256	6.02	5.67	1.5×10^{-5}	1.168	3.03
		6 m	0.0069	22.00	21.60	1.6×10^{-6}	0.559	0.0239	6.64	6.15	1.4×10^{-5}	1.223	3.31
	Apical	24 h	0.0068	22.42	22.09	1.1×10^{-6}	0.456	0.0225	7.03	6.53	1.1×10^{-5}	1.234	3.19
		6 m	0.0065	23.37	23.03	7.3×10^{-7}	0.438	0.0250	6.32	5.87	1.3×10^{-5}	1.229	3.70
Undoped-NPs	Cervical	24 h	0.0070	22.06	21.60	1.2×10^{-6}	0.454	0.0267	6.01	5.65	1.6×10^{-5}	1.232	3.67
		6 m	0.0082	18.17	17.78	1.5×10^{-6}	0.489	0.0244	6.41	6.02	1.5×10^{-5}	1.180	2.83
	Apical	24 h	0.0068	21.87	21.32	1.1×10^{-6}	0.442	0.0254	6.07	5.72	1.5×10^{-5}	1.217	3.60
		6 m	0.0062	23.54	23.12	7.2×10^{-7}	0.465	0.0242	6.40	5.95	1.5×10^{-5}	1.240	3.67
ML-NPs	Cervical	24 h	0.0064	23.26	22.68	1.0×10^{-6}	0.421	0.0216	7.15	6.73	1.1×10^{-5}	0.912	3.25
		6 m	0.0071	20.91	20.39	1.2×10^{-6}	0.652	0.0233	6.62	6.24	1.3×10^{-5}	1.105	3.16
	Apical	24 h	0.0066	22.67	22.10	1.0×10^{-6}	0.520	0.0229	6.77	6.38	1.2×10^{-5}	1.057	3.16
		6 m	0.0066	22.57	22.01	1.1×10^{-6}	0.540	0.0225	6.85	6.46	1.2×10^{-5}	1.093	3.29

Abbreviations: NPs: undoped/unloaded nanoparticles; Mel: Melatonin; FWHM, Full-width half-maximum; R_{hkl}: texture.

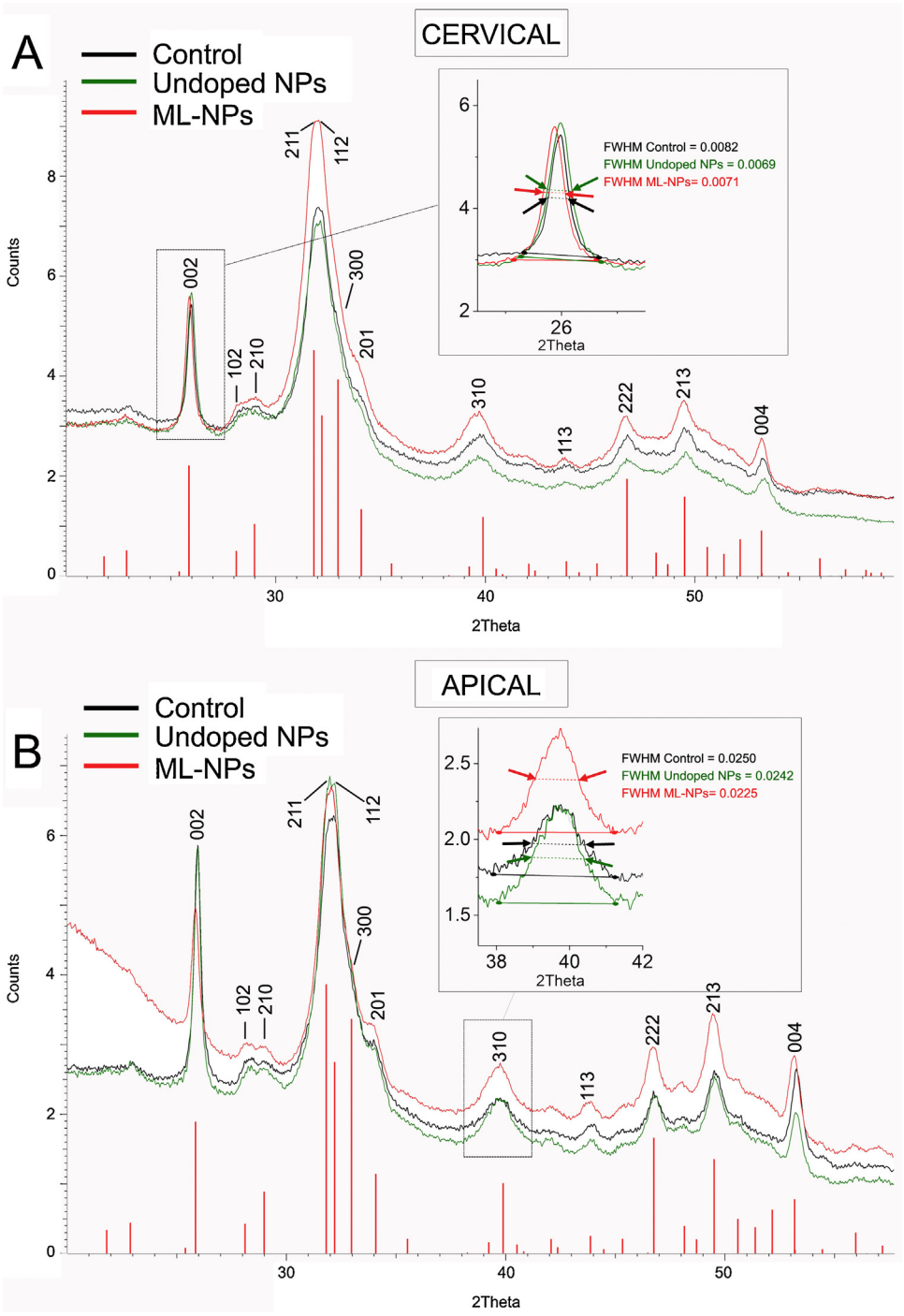

Fig. 3 – Refined μXRD^2 profiles of the inner zones of cervical (A) and apical (B) root dentin after 6 m of SBFS storage of the control, undoped NPs and ML-NPs groups. Vertical bars indicate HAp peaks.

preserved its original mechanical performance over time, but dentin samples treated without NPs decreased their nanohardness (*Hi*) values at 6 m time point. Therefore, the decrease of the *Hi* in dentin specimens without NPs and in apical dentin treated with undoped-NPs may be interpreted as a sight of dentin demineralization and further degradation, indicating scarce remineralization potential at the intrafibrillar part [20,39] after 6 m of storage. Structural porosity, demineralization and collagen degradation are closely related [40]. Thereby, though both types of NPs provided similar values of *Hi* at 6 m storage, ML-NPs can be considered as a drug of long-lasting or durable effect, meanwhile undoped NPs provoked a treatment of unstable or degraded effect (Fig. 2). As a consequence, the null hypothesis that ML-NPs application did not affect, at the short term or overtime nanohardness, crystal morphology and structure of radicular dentin must be partially rejected.

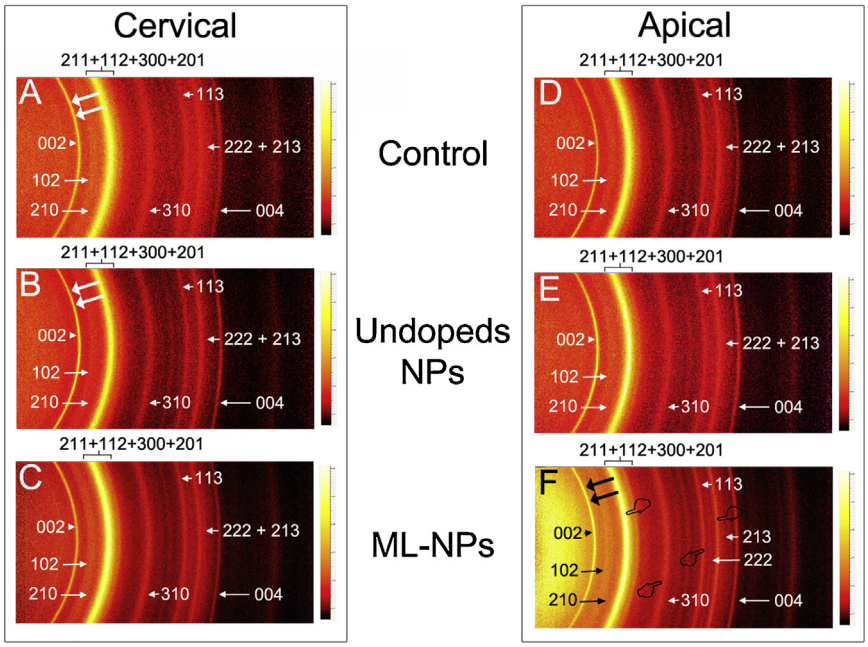

Fig. 4 – The Debye–Scherrer rings are observed in insets (A) and (D) (AH Plus/control), (B) and (E) (Undoped NPs), (C) and (F) (ML-NPs). Double arrows and pointers indicate week and strong diffraction rings, respectively.

In a previous work [12], the release profile of melatonin has been studied, and it was found that the concentration of melatonin immobilised on the particles surface is around 10% (10/90, w/w, NPs/Melatonin). It has been done the following FTIR spectra: Nanoparticles without melatonin (NPs), Nanoparticles functionalised with melatonin (ML-NPs), and melatonin (Fig. S2). But due to the low concentration of melatonin on the particles surface (10/90, w/w, NPs/Melatonin), the intensity of the characteristic FTIR-bands of melatonin: (1) Amine: $NH_{tension}$ = 3300–3500 cm^{-1}, $NH_{deformation}$ = 1500–1640 cm^{-1}, (2) Amide: $NH_{tension}$ = 3180–3500 cm^{-1}, $NH_{deformation}$ = 1500–1650 cm^{-1}, $C{=}O_{tension}$ = 1600–1680 cm^{-1}, is much lower than the intensity of the FTIR-bands of NPs: (1) Alcohol (OH) = 3300–3500 cm^{-1}, (2) Carboxylic acid: $OH_{tension}$ = 2400–3400 cm^{-1}, $OH_{deformation}$ = 2400–3400 cm^{-1}, $C{=}O_{tension}$ = 1700–1750 cm^{-1}, $C{-}O_{tension}$ = 1200–1320 cm^{-1}, (3) Ester (C=O) = 1600–1750 cm^{-1}. Therefore, due to the overlapping between the FTIR-bands of the melatonin (low intensity: 10/90, w/w, Melatonin/NPs) and the FTIR-bands of the NPs (high intensity), the amine and amide groups of melatonin cannot be identified in the FTIR spectrum of ML-NPs (Fig. S2).

Concerning the melatonin liberation profile curve, the highest melatonin liberation was produced at the first 24 h. Then, the expected effect needs to be evaluated at this time-point and the long-term effect (6 m) is also crucial, to appreciate the durability of the impact produced by melatonin [12]. The presence of ML also conditioned the high PDI values (0.230) that were obtained in the present research when ML-NPs were used. Particle accumulation is less likely to happen when the zeta potential is high. Electrostatic stability with zeta potential (ζ) higher than -30 mV is desirable, as it engenders physical stability [30]. In our research, ζ was 38.5 mV, that prevents particles from accumulation [30]. This fact was corroborated after TEM observations (Fig. 1), in the present research.

Crystallinity strongly influences the mechanical performance of minerals [41], enhancing their clinical role. Crystallinity can be understood as the grade of long-range command in materials. The FWHM of the XRD profile is used to characterize different material properties and surface integrity features, and it is sensitive to the variation in microstructure and stress–strain accumulation in the material [42].

Then, the presence of hydroxyapatite crystals with low FWHM values, determines high crystallinity which suggests a moderately lower degree of substitutions and imperfection. In general, higher degree of mineral crystallinity is correlated with narrower spectral peak width [43]. Higher crystallinity denoted improved crystallographic, as narrower peaks advocate minor essential disparity in angles and distances [44]. Otherwise, the relationship between poor crystallinity and peak broadening [45] indicates non-stoichiometry, amorphous phase and existence of higher amounts of impurities [46]. Poor crystallinity, broadening of the Bragg peaks, and overlapping of the diffraction peaks are commonly associated and would make the phase identification ambiguous. To avoid this overlapping 002 and 310 Bragg peaks were used, as they do not overlap [47], though the highest peak (112) was also measured and reported in the present research. This is normally linked to lower mechanical properties [48], and to a low chemical stability leading to an ion-rich environment, likely related with an improved bioactivity and increased solubility [49,50]. In line with this assertion, undoped NPs provoked, in general, peak broadening (high FWHM) and poor crystallinity (Table 1) with a decrease of *Hi* over time (Fig. 2). This amorphous state was likely linked to the intake of carbonate into the apatite crystal [51].

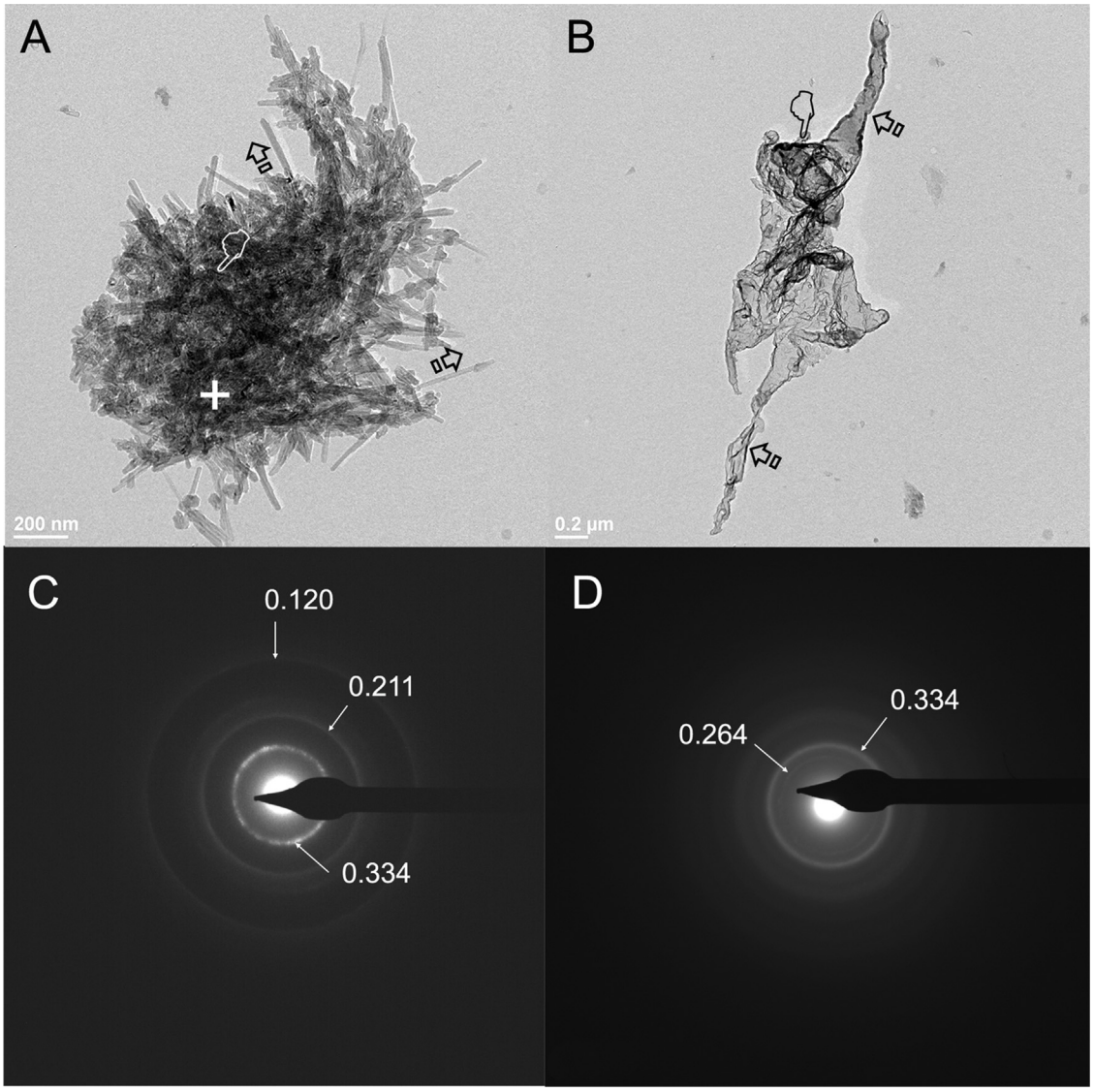

Fig. 5 – (A), Bright-field of an assembly of starry needle-like apatite crystals of cervical root dentin treated with ML-NPs at 24 h of storage. The arrows show the principal direction of the c-axes. The pointer denotes the cut domains with the sectioned crystals seen face-on. (B), Bright-field of an assemblage of block-like and needle-like apatite crystals of apical root dentin treated with ML-NPs at 24 h of storage. Crystals tracked parallel alignment respect to one another (arrows). The particles have multiple domains of nearby aligned crystal arrangements (pointer). (C, D), Show a selected area electron diffraction (SAED) image got by HRTEM of the crystals (+) perceived in (A and B, respectively), at nanoscale. Both depict some relative weak halo rings, specifying amorphous structure and a strong diffraction orbital, signifying the existence of remnant crystallite matter; d-spaces characteristics of hydroxyapatite are indicated.

Diffractography patterns generally transformed from sharper and more crystalline peaks at cervical dentin treated with ML-NPs at 24 h, to broad diffuse peaks after 6 m (Table 1) (Fig. S3). This assures that amorphous stage itself, in nature, is dynamic. The resulted broadening also indicates the state of HAp as ultrafine nano-crystalline [52] at 6 m, that shows the finest biodegradability, biocompatibility and bioactivity when compared with the stoichiometric HAp [49] at 24 h. This crystallization was set after TEM evaluation of HAp, which showed starry needle-like apatite crystals at cervical dentin (Fig. 5A), and parallelized alignments block-like crystals at apical dentin (Fig. 5B). These crystals appeared less criystalline in nature (Fig. 5C, D) than the crystalline polyhedral apatite (Fig. 6A) characteristics of dentin treated with ML-NPs at 6 m. There were observed remarkable halo rings which characterized the crystalline matter (Fig. 6B, F, H), in comparison with specimens treated with undoped NPs. A crystal is made up of small repeat entities called unit cells that are stacked in multiples along all possible axes and this is how a crystal shape is determined. Unit cells for most crystal structures are parallelepipeds or prisms having three sets of parallel faces; one is drawn within the aggregate of spheres which happens to be a cube [53]. In the present research and after using ML-NPs, in bright-field (BF) TEM images, HAp showed poly-

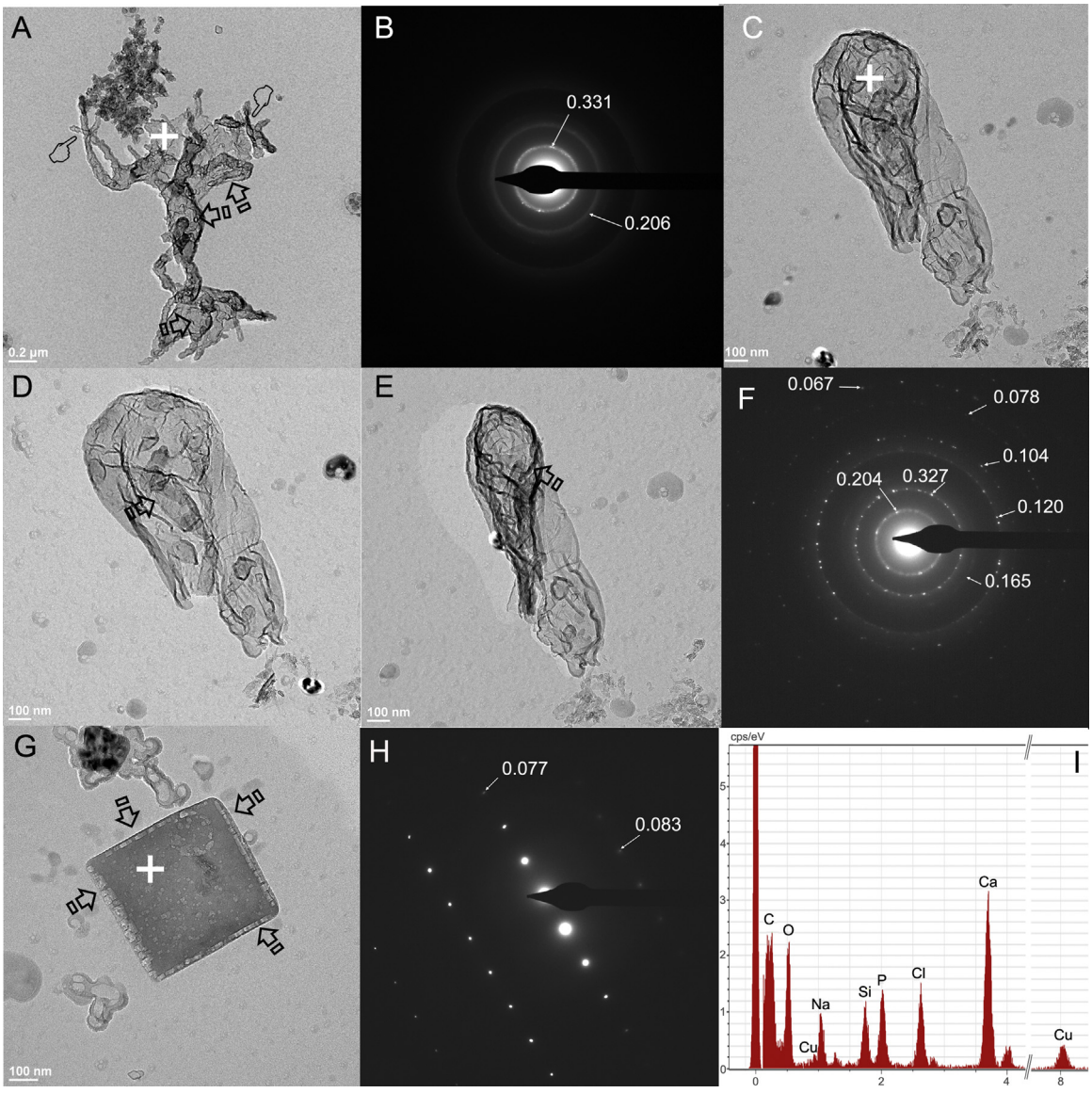

Fig. 6 – (A), Bright-field of an assemblage of block-like and needle-like apatite crystals ordered in three-dimensional agglomerated crystals (pointers) of cervical root dentin treated with ML-NPs at 6 m storage. Some areas of the crystal denoted organization in plate-like polygons (arrows). (B), Shows a particular area electron diffraction (SAED) image got by HRTEM of the crystals (+) observed in (A), at nanoscale. Clear and bright diffraction rings are observed, indicating the existence of crystallite matter. (C, D, E), Bright-field of an assemblage of polyhedral or drop-like shaped apatite crystals, organized in plate-like polygons (arrows), of apical root dentin treated with ML-NPs at 6 m storage. Different tilt angles after tomographic reconstructions, at 0° (C), −15° (D), and +15° (E) are shown by the collage. (F), Shows a specific area electron diffraction (SAED) of the crystals (+) shown in (C), at nanoscale, unveiling a highly polycrystalline structure. (G), Bright-field of an assemblage of a square polygonal block-like apatite of apical root dentin treated with ML-NPs at 6 m time point. The frame of the square figure is composed of an assembly of tiniest and aligned polyhedral grains of apatite crystals (arrows). (H), Selected area electron diffractions (SAED) image obtained by HRTEM of the crystals (+) observed in (G) shown at microscale. They exhibit clear lined up bright spots and diffraction *d* spacing values of submicron size crystals (nm), correlative with crystalline matter. (I), Representative Energy-dispersive X-ray spectroscopy (EDX) of the crystals (+) observed in (G) showing the nanometer-sized apatite composition of calcium and phosphate as part of the elemental analysis; d-spaces characteristics of hydroxyapatite are indicated in B, F and H.

hedral (Fig. 6A), square polygonal block-like apatite (Fig. 6G) or drop-like apatite crystals (Fig. 6C). Thereby, the null hypothesis must be again, partially rejected. Previously, crystallinity not only has become associated to high mechanical properties [49], but with maturity [54] and specific crystallites morphology as drop/rounded-like shaped crystals, polyhedral or even polygons plate-like [46]. When ML was used, polycrystalline lattices were noticed, appearing transparent (Fig. 6D)

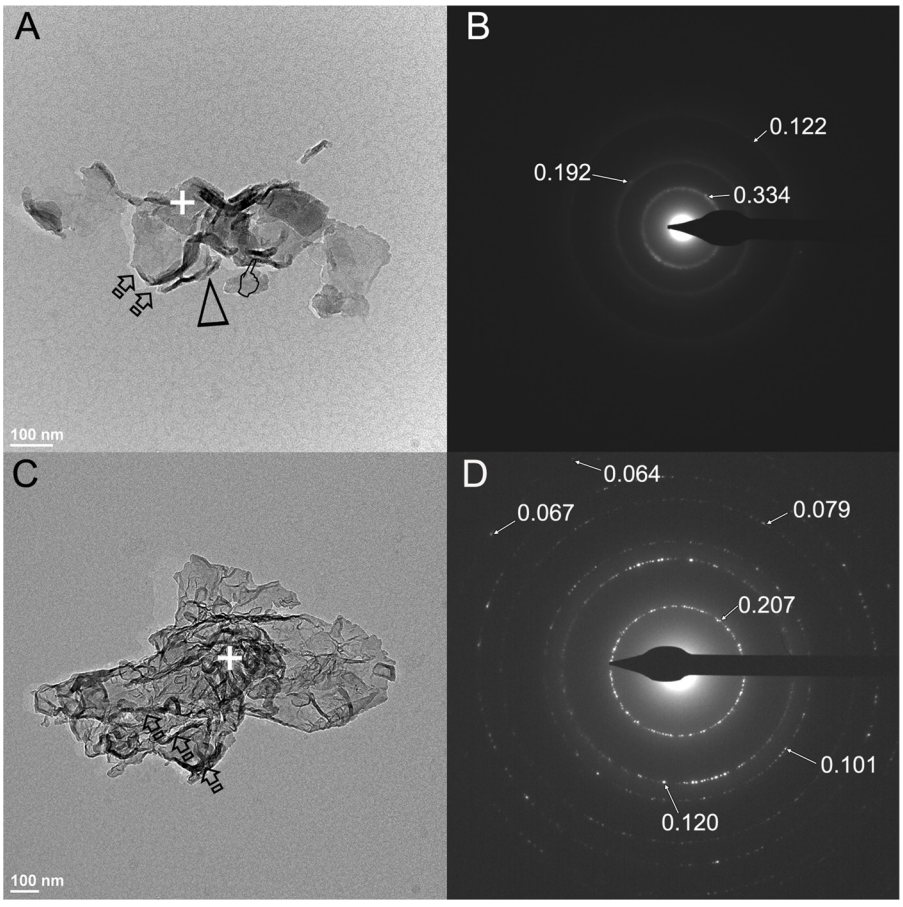

Fig. 7 – (A), Bright-field of an assemblage of polymorph/polyhedral apatite crystals formed by plate-like overlapped crystals (arrows) of cervical root dentin treated with AH Plus at 6 m storage. Aligned crystal arrays may be shown (pointer). Some areas of the crystal denoted organization in plate-like polygons (arrowhead). At cervical dentin, the plate-like apatite minerals of the nanometer-sized particles with poor crystallinity and diffuse halos were adverted (B). This image was obtained by HRTEM of the crystals (+) observed in (A), at microscale. (C), Bright-field of an assemblage of block-like apatite of apical root dentin treated with undoped NPs at 6 m time point, showing the polyhedral apatite presence of the overlapped crystallites (arrows). (D), Selected area electron diffractions (SAED) image got by HRTEM of the crystals (+) observed in C, shown at microscale. They unveil lined up bright spots in junction with diffuse halo rings which denote relative amorphization; d-spaces characteristics of hydroxyapatite are indicated in B and D.

and stable for tilt series acquisition (Fig. 6C, D, E). Profiles of XRD analysis stated higher intensities of ML-NPs treated specimens, denoting high crystallinity and maturity [54], that responds affirmatively to the research question. At 002 peak and cervical dentin (Fig. 3A), and at 211 and 112 peaks at apical dentin (Fig. 3B), diffractography unveiled HAp with remarkable presence (red vertical bars) of sharp and narrow peaks. Similarly, brighter Debye–Scherrer rings were seen at the analysis of diffractions, *i.e.*, greater crystallinity, than in the other specimens when using ML-NPs (Fig. 4F).

The morphology and dimensions of the formed HAp crystals may affect the mechanical properties. In calcified tissues, wider and shorter crystallites are linked to high crystallinity, maturity and mineralization of the new HAp [36]. The crystallite size resulting from Eqs. (1) and (2), is not necessarily the same as apatite particle size, and is considered as the coherently diffracting domains size [22,56]. Table 1 reports a qualitative assessment of the crystallite size. $\tau 002$ (*H*) means crystallite size along the *c*-axis; $\tau 310$ (*L*) denotes the crystallite size mean perpendicular to it [57]. The Scherrer equation, that determines the crystallite thickness, reflects equivalent width data (6.02 nm in the control group, (Table 1) with those attained by Kinney et al. [58] who stated ~5.0 nm thickness. Therefore, considering the present outcomes, (*i*) an association between both contraction along the *c*-axis in cervical dentin treated with ML-NPs and higher crystallinity can be established; (*ii*) it can be assumed that the highest crystallites thickness, at any kind of dentin treated with ML-NPs at 6 m (6.62-cervical and 6.85-apical nm, respectively) (Table 1), complies with a major maturity and mineralization in dentin specimens treated with ML-NPs [12].

Multiple stress concentration, strain and deformations occur at cervical root dentin [59], meanwhile apical dentin has shown the maximal tensile strength and a strong reduction of fracture strength after instrumentation [60,61]. The applied Scherrer–Wilson equation measuring the grain size showed

that dentin crystals turned into smaller (~1.05-fold) in apical dentin treated with ML-NPs (22.01 nm) than in samples treated with undoped NPs (23.12 nm) (Table 1), at (002) reflections. In cervical dentin, and at (310) reflections it did occur the opposite (Table 1). Most strain was concentrated in apical root dentin treated with AH Plus and undoped NPs (7.2 and 7.3 $\times 10^{-7}$, respectively), in 002 plane. In 310 plane similar performance, though with lower strain values, was attained (Table 1). The strain distribution indicates the stiffness of the tooth as strength bearing tissue at biting [24]. It is speculated that these bigger strain data accounted for the peaks broadening (0.0242) in spite of the lowest grain size (6.40 nm) [57] at 310 plane after 6 m of storage. The influence of the strain to the broadening of the peaks will also condition the different mean crystallite sizes [57] (Fig. 7B, D), *i.e.,* lesser crystallite size (Fig. 7A, B) with augmented microstrain data and lattice distortion [45,62] (Table 1). Distortion of the phosphate tetrahedron is correlated with the well-known lattice disorder caused by the carbonate for phosphate (β-type) substitution in HAp, named as 'carbonate substitution problem' [47]. This was the characteristic performance of specimens treated with undoped NPs at any kind of dentin. At these locations, FWHM and microstrain have shown the highest values (Table 1).

The alignment and orientation of the apatite crystals are related with the mechanical behavior of macroscopic dentin [63]. Texture correlates with the supply of crystallographic alignment of a polycrystalline specimen. Texture highly determines the materials performance, as the resistance to crack [64]. Therefore, texture indices (R_{hkl}) were calculated. Random orientation is established when $R \approx 1$ [36,49]. Thereby, it may be advocated that dentin treated with ML-NPs has shown the most randomly oriented polycrystalline lattices within the HAp structure, at cervical (1.105) and apical dentin (1.093), at 6 m time point and 310 plane (Table 1). These crystal nets are associated to highly crystalline structures with low solubility and high stability of the new minerals [48]. The preferred orientation of the crystallites are indicated by indices greater than 1 [36,49]. At 002 reflections, all measurements were below 1.0 ($R < 1$), but all groups attained minor variation than at 310 reflection, with occasional nano-degradation [49,65]. This indicates scarce gradation in texture at dentin structure, providing poor hardness and stress-bearing capability [49].

Melatonin is a potent anti-inflammatory agent as it partially neutralizes reactive oxygen species (ROS), in which OH^- plays a pivotal role [66]. It has been further proposed that when the crystal size decreases, the grade of hydroxylation or the integration of OH^- in the HAp also diminishes [49]. ML-NPs produced the highest crystallite size, in general (Table 1). Thereby, it is speculated that the new crystallites created after ML-NPs application will integrate OH- radicals into the apatite structure. Crystal order may be inducted by a gain of OH^- in nanocrystalline HAp. It has been demonstrated that the incorporation OH^- radicals to apatite, in order to form HAp, follows a crystallization pathway via an amorphous calcium phosphate (ACP) precursor [67,68]. However, the transformation mechanism of the ACP precursor to HAp remains unknown and it is a subject of active debate and future research [69]. It may be considered as a limitation of the current research. The ACP transformation into HAp, following the classical crystallization theory, is governed by chemical potentials, normally by dissolution-reprecipitation pathway. It has been previously described that the presence of additives in this process, can modify the kinetics of transformation of APC into HAp [69]. Thereby, it is speculated that the new crystallites created after ML-NPs application will integrate OH^- radicals into the apatite structure, forming HAp. The polar nature of the HAp may be favored by the OH^- ions which are more readily incorporated into the apatite with a big lattice. The high degree of alignment of crystallites is clearly determined by polarity. At the same time, a relative degree of crystal disorder coming from the random alignment of crystallites is due to the lack of polarity and OH^- produced by the ML effects. It seems that nature carry out some disorder of crystals by changing the OH^- concentration to improve the facility of biological apatite to accomplish their functions [70]. Further research to clarify this point is required. Thereby, it may be assumed that the apatite crystals inducted after ML-NPs application, at 6 m of storage, do have a relative degree of mixed preferred and randomly oriented crystallites that provide both amorphous and crystalline features to the new minerals, elementally composed of calcium and phosphate (Fig. 6I). Even more, as observed in the presented research, as demonstrated by the broadening of the crystals due to ML treated NPs, are not only the measure of the degree of mineralization. There are other connected factors such as higher numbers of planar carbonate groups substituting for the tetrahedral phosphate ions in the apatite structure that account for the increased crystal structure disorder and reduction of the crystallinity [47]. Future and complementary research should be provided in this line. The purpose of the present research was achieved in the current manuscript, as undoped NPs provoked peak broadening (high FWHM) and poor crystallinity with a decrease of nanohardness over time. This amorphous state was likely associated to the intake of carbonate into the apatite crystal. The amorphization process created crystals imperfections, *i.e.,* lesser crystallite size and lattice distortion with augmented microstrain data; this was the characteristic performance of specimens treated with undoped NPs at any kind of dentin. Decrease of the a-lattice parameter in amorphous (carbonate) apatite is associated with an increase in carbonate content [47]. This is biologically important, as the raise in carbonate content involves an augmentation in solubility of the HAp, and as result, the formation of ACP that change the mineral composition [47]. Nevertheless, most strain was concentrated in apical root dentin treated with AH Plus and undoped NPs. On the other hand, samples treated with ML-NPs showed HAp with remarkable presence of sharp and narrow peaks through diffractography. Brighter Debye–Scherrer rings were seen at the analysis of diffractions, *i.e.*, higher crystallinity. The highest crystallites thickness, at any kind of dentin treated with ML-NPs at 6 m, complies with a major maturity and mineralization in dentin specimens treated with ML-NPs. These crystal nets are associated to highly crystalline structures with low solubility and high stability of the new minerals.

These are the only existing outcomes from both XRD and TEM/EDX/SAED joined methodologies applicable to evaluate radicular dentin submitted to ML-NPs treatment. Dark-field TEM and Scanning Transmission Electron Microscopy should be methodologically integrated, for future approaches of

research. It is a recognized limitation of the present research. Cervical root dentin is a site of potential failure due to stress concentration, strain and deformation [59]. Meanwhile, apical dentin has shown the maximal tensile strength and a strong reduction of fracture strength after instrumentation [60,61]. Therefore, the use of ML-NPs should be applied in endodontics, as they reinforce both cervical and apical radicular dentin in comparison with both the control and undoped NPs groups which showed a *Hi* decreased over time (Fig. 2). In summary, application of ML-NPs in radicular dentin has been greatly effective. High hydrophilicity, smaller size of NPs and controlled release of ML may have contributed to the analyzed performance of these ML nanocarriers. The hydrophobicity property of ML may also have facilitated its release from the NPs in the root dentin [30].

5. Conclusions

Dentin treated with ML-NPs preserved its original mechanical performance over time attaining higher crystallinity, being these crystals organized with randomly oriented lattices. However, undoped NPs induced HAp amorphization (poor crystallinity, high impurities degree, imperfections and non-stoichiometric crystals).

Declaration of Competing Interest

The authors report no declarations of interest.

Acknowledgements

This work was funded by the Ministry of Economy and Competitiveness and European Regional Development Fund (MINECO/AEI/FEDER/UE) Project number PID2020-114694RB-I00. Funding for open access charge: University of Granada / CBUA.

Appendix A. Supplementary data

Supplementary material related to this article can be found, in the online version, at doi:https://doi.org/10.1016/j.dental.2021.09.001.

REFERENCES

[1] Sismanoglu S, Ercal P. Dentin-pulp tissue regeneration approaches in dentistry: an overview and current trends. In: Turksen K, editor. Cell biology and translational medicine, volume 10: stem cells in tissue regeneration. Cham: Springer International Publishing; 2020. p. 79–103, http://dx.doi.org/10.1007/5584_2020_578.

[2] Vengerfeldt V, Mändar R, Saag M, Piir A, Kullisaar T. Oxidative stress in patients with endodontic pathologies. J Pain Res 2017;10:2031–40, http://dx.doi.org/10.2147/JPR.S141366.

[3] Giraud T, Jeanneau C, Bergmann M, Laurent P, About I. Tricalcium silicate capping materials modulate pulp healing and inflammatory activity in vitro. J Endod 2018;44:1686–91, http://dx.doi.org/10.1016/j.joen.2018.06.009.

[4] Meenakshi SS, Malaiappan S. Role of melatonin in periodontal disease — a systematic review. Indian J Dent Res 2020;31:593–600, http://dx.doi.org/10.4103/ijdr.IJDR_227_18.

[5] Shino H, Hasuike A, Arai Y, Honda M, Isokawa K, Sato S. Melatonin enhances vertical bone augmentation in rat calvaria secluded spaces. Med Oral Patol Oral Cir Bucal 2016;21:e122–126, http://dx.doi.org/10.4317/medoral.20904.

[6] Acuña-Castroviejo D, Rahim I, Acuña-Fernández C, Fernández-Ortiz M, Solera-Marín J, Sayed RKA, et al. Melatonin, clock genes and mitochondria in sepsis. Cell Mol Life Sci 2017;74:3965–87, http://dx.doi.org/10.1007/s00018-017-2610-1.

[7] Liu J, Huang F, He H-W. Melatonin effects on hard tissues: bone and tooth. Int J Mol Sci 2013;14:10063–74, http://dx.doi.org/10.3390/ijms140510063.

[8] Huojia M, Muraoka N, Yoshizaki K, Fukumoto S, Nakashima M, Akamine A, et al. TGF-beta3 induces ectopic mineralization in fetal mouse dental pulp during tooth germ development. Dev Growth Differ 2005;47:141–52, http://dx.doi.org/10.1111/j.1440-169x.2005.00790.x.

[9] Scheller EL, Chang J, Wang CY. Wnt/beta-catenin inhibits dental pulp stem cell differentiation. J Dent Res 2008;87:126–30, http://dx.doi.org/10.1177/154405910808700206.

[10] Neitzel J, Rasband M. Cell Communication | Learn Science at Scitable n.d. https://www.nature.com/scitable/topic/cell-communication-14122659/ [Accessed 23 June 2021].

[11] Jordan JD, Landau EM, Iyengar R. Signaling networks: the origins of cellular multitasking. Cell 2000;103:193–200.

[12] Toledano M, Aguilera FS, Osorio E, Toledano-Osorio M, Escames G, Medina-Castillo AL, et al. Melatonin-doped polymeric nanoparticles reinforce and remineralize radicular dentin: morpho-histological, chemical and biomechanical studies. Dent Mater 2021;37:1107–20, http://dx.doi.org/10.1016/j.dental.2021.03.007.

[13] Santos RMD, Marani F, Chiba FY, Mattera MS de LC, Tsosura TVS, Tessarin GWL, et al. Melatonin promotes reduction in TNF levels and improves the lipid profile and insulin sensitivity in pinealectomized rats with periodontal disease. Life Sci 2018;213:32–9, http://dx.doi.org/10.1016/j.lfs.2018.09.056.

[14] Toledano M, Osorio E, Aguilera FS, Muñoz-Soto E, Toledano-Osorio M, López-López MT, et al. Polymeric nanoparticles for endodontic therapy. J Mech Behav Biomed Mater 2020;103:103606, http://dx.doi.org/10.1016/j.jmbbm.2019.103606.

[15] Toledano-Osorio M, Osorio R, Aguilera FS, Medina-Castillo AL, Toledano M, Osorio E, et al. Polymeric nanoparticles protect the resin-dentin bonded interface from cariogenic biofilm degradation. Acta Biomater 2020;111:316–26, http://dx.doi.org/10.1016/j.actbio.2020.05.002.

[16] Köse O, Arabaci T, Kizildag A, Erdemci B, Eminoğlu DÖ, Gedikli S, et al. Melatonin prevents radiation-induced oxidative stress and periodontal tissue breakdown in irradiated rats with experimental periodontitis. J Periodont Res 2017;52:438–46, http://dx.doi.org/10.1111/jre.12409.

[17] Fernández-Ortiz M, Sayed RKA, Fernández-Martínez J, Cionfrini A, Aranda-Martínez P, Escames G, et al. Melatonin/Nrf2/NLRP3 connection in mouse heart mitochondria during aging. Antioxidants (Basel) 2020;9, http://dx.doi.org/10.3390/antiox9121187.

[18] Fernández-Gil B, Moneim AEA, Ortiz F, Shen Y-Q, Soto-Mercado V, Mendivil-Perez M, et al. Melatonin protects rats from radiotherapy-induced small intestine toxicity. PLoS One 2017;12, http://dx.doi.org/10.1371/journal.pone.0174474.

[19] Bertassoni LE, Habelitz S, Pugach M, Soares PC, Marshall SJ, Marshall GW. Evaluation of surface structural and mechanical changes following remineralization of dentin. Scanning 2010;32:312–9, http://dx.doi.org/10.1002/sca.20199.
[20] Kinney JH, Habelitz S, Marshall SJ, Marshall GW. The importance of intrafibrillar mineralization of collagen on the mechanical properties of dentin. J Dent Res 2003;82:957–61, http://dx.doi.org/10.1177/154405910308201204.
[21] Bertassoni LE, Orgel JPR, Antipova O, Swain MV. The dentin organic matrix — limitations of restorative dentistry hidden on the nanometer scale. Acta Biomater 2012;8:2419–33, http://dx.doi.org/10.1016/j.actbio.2012.02.022.
[22] Toledano M, Aguilera FS, López-López MT, Osorio E, Toledano-Osorio M, Osorio R. Zinc-containing restorations create amorphous biogenic apatite at the carious dentin interface: a X-ray diffraction (XRD) crystal lattice analysis. Microsc Microanal 2016;22:1034–46, http://dx.doi.org/10.1017/S1431927616011697.
[23] Wang F, Guo E, Song E, Zhao P, Liu J. Structure and properties of bone-like-nanohydroxyapatite/gelatin/polyvinyl alcohol composites. Adv Biosci Biotechnol 2010;1, http://dx.doi.org/10.4236/ABB.2010.13026.
[24] Fujisaki K, Todoh M, Niida A, Shibuya R, Kitami S, Tadano S. Orientation and deformation of mineral crystals in tooth surfaces. J Mech Behav Biomed Mater 2012;10:176–82, http://dx.doi.org/10.1016/j.jmbbm.2012.02.025.
[25] Kinney JH, Nalla RK, Pople JA, Breunig TM, Ritchie RO. Age-related transparent root dentin: mineral concentration, crystallite size, and mechanical properties. Biomaterials 2005;26:3363–76, http://dx.doi.org/10.1016/j.biomaterials.2004.09.004.
[26] Bertassoni LE, Stankoska K, Swain MV. Insights into the structure and composition of the peritubular dentin organic matrix and the lamina limitans. Micron 2012;43:229–36, http://dx.doi.org/10.1016/j.micron.2011.08.003.
[27] Toledano-Osorio M, Aguilera FS, Osorio R, Muñoz-Soto E, Pérez-Álvarez MC, López-López MT, et al. Hydroxyapatite-based cements induce different apatite formation in radicular dentin. Dent Mater 2020;36:167–78, http://dx.doi.org/10.1016/j.dental.2019.11.023.
[28] Medina-Castillo AL, Fernandez-Sanchez JF, Segura-Carretero A, Fernandez-Gutierrez A. Micrometer and submicrometer particles prepared by precipitation polymerization: thermodynamic model and experimental evidence of the relation between Flory's parameter and particle size. Macromolecules 2010;43:5804–13, http://dx.doi.org/10.1021/ma100841c.
[29] Schaffazick SR, Pohlmann AR, Mezzalira G, Guterres SS. Development of nanocapsule suspensions and nanocapsule spray-dried powders containing melatonin. J Braz Chem Soc 2006;17:562–9, http://dx.doi.org/10.1590/S0103-50532006000300020.
[30] Noori Siahdasht F, Farhadian N, Karimi M, Hafizi L. Enhanced delivery of melatonin loaded nanostructured lipid carriers during in vitro fertilization: NLC formulation, optimization and IVF efficacy. RSC Adv 2020;10:9462–75, http://dx.doi.org/10.1039/C9RA10867J.
[31] Rodriguez-Navarro C, Burgos Cara A, Elert K, Putnis CV, Ruiz-Agudo E. Direct nanoscale imaging reveals the growth of calcite crystals via amorphous nanoparticles. Cryst Growth Des 2016;16:1850–60, http://dx.doi.org/10.1021/acs.cgd.5b01180.
[32] Toledano M, Muñoz-Soto E, Aguilera FS, Osorio E, González-Rodríguez MP, Pérez-Álvarez MC, et al. A zinc oxide-modified hydroxyapatite-based cement favored sealing ability in endodontically treated teeth. J Dent 2019;88:103162, http://dx.doi.org/10.1016/j.jdent.2019.06.009.
[33] Mestres G, Aguilera FS, Manzanares N, Sauro S, Osorio R, Toledano M, et al. Magnesium phosphate cements for endodontic applications with improved long-term sealing ability. Int Endod J 2014;47:127–39, http://dx.doi.org/10.1111/iej.12123.
[34] Rodriguez-Navarro AB. Registering pole figures using an X-ray single-crystal diffractometer equipped with an area detector. J Appl Cryst 2007;40:631–4, http://dx.doi.org/10.1107/S0021889807014574.
[35] Perales F, Agulló-Rueda F, Lamela J, de las Heras C. Optical and structural properties of Sb2S3/MgF2 multilayers for laser applications. J Phys Appl Phys 2008;41, http://dx.doi.org/10.1088/0022-3727/41/4/045403.
[36] Xue J, Zavgorodniy AV, Kennedy BJ, Swain MV, Li W. X-ray microdiffraction, TEM characterization and texture analysis of human dentin and enamel. J Microsc 2013;251:144–53, http://dx.doi.org/10.1111/jmi.12053.
[37] Martinez-Ruiz F, Paytan A, Gonzalez-Muñoz MT, Jroundi F, Abad MM, Lam PJ, et al. Barite formation in the ocean: origin of amorphous and crystalline precipitates. Chem Geol 2019;511:441–51, http://dx.doi.org/10.1016/j.chemgeo.2018.09.011.
[39] Toledano M, Osorio E, Cabello I, Osorio R. Early dentine remineralisation: morpho-mechanical assessment. J Dent 2014;42:384–94, http://dx.doi.org/10.1016/j.jdent.2014.01.012.
[40] Toledano M, Osorio R, Osorio E, Medina-Castillo AL, Toledano-Osorio M, Aguilera FS. Ions-modified nanoparticles affect functional remineralization and energy dissipation through the resin-dentin interface. J Mech Behav Biomed Mater 2017;68:62–79, http://dx.doi.org/10.1016/j.jmbbm.2017.01.026.
[41] Seyedmahmoud R, McGuire JD, Wang Y, Thiagarajan G, Walker MP. The interrelationship of microstructure and hardness of human coronal dentin using reference point indentation technique and micro-Raman spectroscopy. Dent Mater 2017;33:1069–74, http://dx.doi.org/10.1016/j.dental.2017.07.005.
[42] Vashista M, Paul S. Correlation between full width at half maximum (FWHM) of XRD peak with residual stress on ground surfaces. Philos Mag 2012;92:4194–204, http://dx.doi.org/10.1080/14786435.2012.704429.
[43] Karan K, Yao X, Xu C, Wang Y. Chemical profile of the dentin substrate in non-carious cervical lesions. Dent Mater 2009;25:1205–12, http://dx.doi.org/10.1016/j.dental.2009.04.006.
[44] Schwartz AG, Pasteris JD, Genin GM, Daulton TL, Thomopoulos S. Mineral distributions at the developing tendon enthesis. PLoS One 2012;7:e48630, http://dx.doi.org/10.1371/journal.pone.0048630.
[45] Zhang Z, Zhou F, Lavernia EJ. On the analysis of grain size in bulk nanocrystalline materials via x-ray diffraction. Metall Mater Trans A 2003;34:1349–55, http://dx.doi.org/10.1007/s11661-003-0246-2.
[46] Toledano M, Aguilera FS, Osorio E, López-López MT, Cabello I, Toledano-Osorio M, et al. Submicron-to-nanoscale structure characterization and organization of crystals in dentin bioapatites. RSC Adv 2016;6:45265–78, http://dx.doi.org/10.1039/C6RA02373H.
[47] Leventouri Th, Antonakos A, Kyriacou A, Venturelli R, Liarokapis E, Perdikatsis V. Crystal structure studies of human dental apatite as a function of age. Int J Biomater 2009;2009:698547, http://dx.doi.org/10.1155/2009/698547.
[48] Moshaverinia A, Ansari S, Moshaverinia M, Roohpour N, Darr JA, Rehman I. Effects of incorporation of hydroxyapatite and fluoroapatite nanobioceramics into conventional glass ionomer cements (GIC). Acta Biomater 2008;4:432–40, http://dx.doi.org/10.1016/j.actbio.2007.07.011.

[49] Low I-M. Depth-profiling of crystal structure, texture, and microhardness in a functionally graded tooth enamel. J Am Ceram Soc 2004;87:2125–31, http://dx.doi.org/10.1111/j.1151-2916.2004.tb06369.x.
[50] Osorio R, Cabello I, Toledano M. Bioactivity of zinc-doped dental adhesives. J Dent 2014;42:403–12, http://dx.doi.org/10.1016/j.jdent.2013.12.006.
[51] Toledano M, Osorio E, Aguilera FS, Cabello I, Toledano-Osorio M, Osorio R. Ex vivo detection and characterization of remineralized carious dentin, by nanoindentation and single point Raman spectroscopy, after amalgam restoration. J Raman Spectrosc 2017;48:384–92, http://dx.doi.org/10.1002/jrs.5055.
[52] Liu Y, Huang J, Li H. Synthesis of hydroxyapatite-reduced graphite oxide nanocomposites for biomedical applications: oriented nucleation and epitaxial growth of hydroxyapatite. J Mater Chem B 2013;1:1826–34, http://dx.doi.org/10.1039/c3tb00531c.
[53] Callister WD, Rethwisch DG. Materials science and engineering: an introduction. 8th ed. Wiley and sons; 2010. Wiley. 8th ed.
[54] Cutando A, Gómez-Moreno G, Arana C, Muñoz F, Lopez-Peña M, Stephenson J, et al. Melatonin stimulates osteointegration of dental implants. J Pineal Res 2008;45:174–9, http://dx.doi.org/10.1111/j.1600-079X.2008.00573.x.
[56] Bindu P, Thomas S. Estimation of lattice strain in ZnO nanoparticles: X-ray peak profile analysis. J Theor Appl Phys 2014;8:123–34, http://dx.doi.org/10.1007/s40094-014-0141-9.
[57] Bigi A, Boanini E, Gazzano M, Kojdecki MA, Rubini K. Microstructural investigation of hydroxyapatite–polyelectrolyte composites. J Mater Chem 2004;14:274–9, http://dx.doi.org/10.1039/B308687A.
[58] Kinney JH, Oliveira J, Haupt DL, Marshall GW, Marshall SJ. The spatial arrangement of tubules in human dentin. J Mater Sci Mater Med 2001;12:743–51, http://dx.doi.org/10.1023/a:1011232912734.
[59] Kaushik M, Kumar U, Sharma R, Mehra N, Rathi A. Stress distribution in endodontically treated abfracted mandibular premolar restored with different cements and crowns: a three-dimensional finite element analysis. J Conserv Dent 2018;21:557–61, http://dx.doi.org/10.4103/JCD.JCD_206_18.
[60] Patil P, Banga KS, Pawar AM, Pimple S, Ganeshan R. Influence of root canal obturation using gutta-percha with three different sealers on root reinforcement of endodontically treated teeth. An in vitro comparative study of mandibular incisors. J Conserv Dent 2017;20:241–4, http://dx.doi.org/10.4103/JCD.JCD_233_16.
[61] Brosh T, Metzger Z, Pilo R. Circumferential root strains generated during lateral compaction with stainless steel vs. nickel-titanium finger spreaders. Eur J Oral Sci 2018;126:518–25, http://dx.doi.org/10.1111/eos.12569.
[62] Toledano M, Aguilera FS, Osorio E, Cabello I, Toledano-Osorio M, Osorio R. Functional and molecular structural analysis of dentine interfaces promoted by a Zn-doped self-etching adhesive and an in vitro load cycling model. J Mech Behav Biomed Mater 2015;50:131–49, http://dx.doi.org/10.1016/j.jmbbm.2015.05.026.
[63] Sui T, Sandholzer MA, Baimpas N, Dolbnya IP, Walmsley A, Lumley PJ, et al. Multiscale modelling and diffraction-based characterization of elastic behaviour of human dentine. Acta Biomater 2013;9:7937–47, http://dx.doi.org/10.1016/j.actbio.2013.04.020.
[64] Liss K-D, Bartels A, Schreyer A, Clemens H. High-energy X-rays: a tool for advanced bulk investigations in materials science and physics. Textures Microstruct 2003;35:219–52, http://dx.doi.org/10.1080/07303300310001634952.
[65] Toledano M, Osorio R, Vallecillo-Rivas M, Osorio E, Lynch CD, Aguilera FS, et al. Zn-doping of silicate and hydroxyapatite-based cements: dentin mechanobiology and bioactivity. J Mech Behav Biomed Mater 2020;114:104232, http://dx.doi.org/10.1016/j.jmbbm.2020.104232.
[66] Guerrero-Gironés J, Alcaina-Lorente A, Ortiz-Ruiz C, Ortiz-Ruiz E, Pecci-Lloret MP, Rodríguez-Lozano FJ, et al. Melatonin as an agent for direct pulp-capping treatment. Int J Environ Res Public Health 2020;17, http://dx.doi.org/10.3390/ijerph17031043.
[67] Weiner S, Mahamid J, Politi Y, Ma Y, Addadi L. Overview of the amorphous precursor phase strategy in biomineralization. Front Mater Sci China 2009;3:104, http://dx.doi.org/10.1007/s11706-009-0036-x.
[68] Olszta MJ, Cheng X, Jee SS, Kumar R, Kim Y-Y, Kaufman MJ, et al. Bone structure and formation: a new perspective. Mater Sci Eng R Rep 2007;58:77–116, http://dx.doi.org/10.1016/j.mser.2007.05.001.
[69] Ucar S, Bjørnøy SH, Bassett DC, Strand BL, Sikorski P, Andreassen J-P. Formation of hydroxyapatite via transformation of amorphous calcium phosphate in the presence of alginate additives. Cryst Growth Des 2019;19:7077–87, http://dx.doi.org/10.1021/acs.cgd.9b00887.
[70] Pasteris JD, Wopenka B, Freeman JJ, Rogers K, Valsami-Jones E, van der Houwen JAM, et al. Lack of OH in nanocrystalline apatite as a function of degree of atomic order: implications for bone and biomaterials. Biomaterials 2004;25:229–38, http://dx.doi.org/10.1016/s0142-9612(03)00487-3.